Structural, electronic, and excitonic properties of few-layer SeS$_2$ and TeS$_2$

Jingjing Min,[1] Pingping Han,[1] Xiaoyu Ma,[1] Zaiping Zeng ●,[1,*] Congxin Xia,[2] and Yu Jia[1,3,†]

[1]*Key Laboratory for Special Functional Materials of Ministry of Education,*
Collaborative Innovation Center of Nano Functional Materials and Applications,
and School of Materials Science and Engineering, Henan University, Kaifeng, Henan 475001, China
[2]*College of Physics and Materials Science, Henan Normal University, Xinxiang 453007, China*
[3]*International Laboratory for Quantum Functional Materials of Henan, and School of Physics and Engineering,*
Zhengzhou University, Zhengzhou, Henan 450001, China

High-efficiency optoelectronic devices require materials with suitable band gap, excellent carrier mobility, strong light-matter interaction, and high thermal- and photostability. Herein, we report two layered materials of group VI, namely, SeS$_2$ and TeS$_2$, which meet all those desired criteria. Both materials are stable with 1T-MoS$_2$-like structure, and exhibit in-direct gap semiconducting feature and possess extraordinary electronic transport properties with isotropic carrier mobilities outperforming their MoS$_2$ analog. Using the *GW* approach for determining the quasiparticle electronic structure and Bethe-Salpeter equation accounting for the many-body excitonic effects, the optical properties of both materials have been identified. We find that exciton effects are significant in both materials that is characterized by the large binding energy of 0.66 and 0.84 eV for monolayer SeS$_2$ and TeS$_2$, respectively. The absorption edges lie in the optimal energy window of 1.0–1.5 eV, which enables strong photoabsorption covering the whole visible-light region. Finally and importantly, we demonstrate that the in-direct nature of those materials can be violated by capping them with 2H-MoS$_2$ to form a van der Waals heterostructure, while keeping the gap in the energy favorable region. Those physical and optical characteristics make few-layer SeS$_2$ and TeS$_2$ highly appealing for room-temperature light-emitting devices and, particularly, solar harvesting devices.

I. INTRODUCTION

Since the discovery of graphene, two-dimensional (2D) materials have garnered tremendous interest owing to their superior physical, chemical, and optical properties, and their potential applications in many electronic and optoelectronic devices [1]. After experiencing nearly two-decades fruitful research and development, 2D materials family has been significantly expanded and enriched, including those of groups IV and V [2–4], offering rich material characteristics and functionalities. Our recent discovery of tellurene, a 2D allotrope of tellurium (Te), has further extended the realm of 2D materials to group VI [5]. Unlike those of groups IV and V in which the bulk parentage is usually layered, bulk Te of group VI, however, has a trigonal crystal lattice in which individual helical chains of Te atoms are stacked together by coordinate covalent bonding instead of weak van der Waals interactions [6] and spiral around axes parallel to the [0001] direction at the center and corners of the hexagonal elementary cell [7]. Therefore the formation of the 2D layered material, tellurene, from a nonlayered bulk tellurium is intriguing, and the mechanism of this helix-to-layer transformation has been explored to be a multistep formation process that involves

a concerted motion of many atoms at dislocation defects [8]. Three mechanically stable phases have been identified, i.e., the stable 1T-MoS$_2$-like (α-tellurene), metastable tetragonal (β-tellurene), and 2H-MoS$_2$-like (γ-tellurene) structures. α-tellurene has demonstrated its potential application in far-infrared optoelectronic devices given its narrow band-gap nature [9,10]. The metastable tetragonal phase has been experimentally realized on highly oriented pyrolytic graphite (HOPG) by molecular-beam epitaxy [11], and the γ-tellurene has a metallic feature.

The on-going efforts of the study of 2D materials of group VI are twofold: (i) determine physical properties of the existing 2D materials, (ii) discover new 2D materials to further enrich the group-VI family. The former activities are very dynamic. The electronic and excitonic optical [5,9,12], thermal [13,14] and piezoelectric properties [15], atomic transport properties [16], and spin texture [17] of tellurene have been successively explored [18]. The 2D material of group VI indeed outperforms its bulk parentage in many of those properties. For example, α-tellurene delivers a much larger band gap at the monolayer limit ($\sim$1.31 eV [9]) than its bulk parentage ($\sim$0.336 eV [19]), and its band gap is further tunable with the number of layers in the stack. Furthermore, tellurene also exhibits unusually low thermal conductivity, which is lower than any values ever reported for 2D materials. In stark contrast, the latter activities are rather limited, and only the stable structures of 2D elemental selenium allotropes have been very

*zaiping.zeng@henu.edu.cn
†jiayu@henu.edu.cn

recently screened using a combined particle-swarm optimization (PSO) method with first-principles calculations [20,21].

In this contribution, we have discovered two novel 2D materials of group VI, namely, monolayer SeS_2 and TeS_2, to further expand the 2D family of group VI. Their stable structural properties have been identified using first-principles density functional theory (DFT) calculations. On ground of those stable geometric structures, we have explored their electronic and exctionic optical properties using the state-of-the-art *ab initio* many-body calculations. These newly discovered monolayer materials are found to be of indirect semiconducting nature, and exhibit excellent electronic transport properties with isotropic carrier mobilities, which outperform their 2D MoS_2 counterpart. Remarkably, they exhibit strong optical absorbance in the whole visible-light region, and the absorption edges of these monolayers are further tunable with number of layers in the stack. These characteristics are highly appealing for flexible room-temperature optoelectronic device applications for display and lighting. Finally, we demonstrate that the in-direct nature can be violated via stacking those 2D materials on top of 2D MoS_2 to form a typical van der Waals heterojunction, while keeping the band edge in the visible-light region.

II. COMPUTATIONAL DETAILS

All calculations are performed by employing the Vienna *ab initio* simulation package (VASP) [22–24]. The geometry optimization is carried out based on density functional theory using projected augmented wave (PAW) pseudopotentials, and various functionals for the treatment of exchange-correlation energy, including the local density functional approximation (LDA), the generalized gradient approximation (GGA) [22,25] of the Perdew-Burke-Ernzerhof (PBE) type [26], and the recently proposed strongly constrained and appropriately normed meta-GGA (meta-GGA-SCAN) functional [27]. The positions of atoms in the simulation cell, the lattice parameters, and the corresponding angles are fully relaxed until the atomic force reaches the tolerance of 0.01 eV/Å. The kinetic energy cutoff is chosen as 500 eV and the energy convergence criteria is set to be 10^{-5} eV/cell. The Brillouin zone is sampled using $12 \times 12 \times 1$ Γ-centered Monkhorst-Pack meshes. The 2D Brillouin zone and the high-symmetry k points are shown in Fig. 1. We have included the vdw interactions using the DFT-D2 method of Grimme [28,29].

The quasiparticle band structures are computed using the GW approach. We employ the "one-shot" G_0W_0 approximation based on the optimized structures, and on top of DFT/PBE calculations. After performing a careful convergence test over the cutoff energy for the response function $(E_{\mathrm{cut},GW})$, and the number of bands (N_B), and the k-point sampling, we find that $E_{\mathrm{cut},GW} = 200$ eV, $N_B = 336$, and $12 \times 12 \times 1$ k grid are sufficient to converge both the in-direct and direct quasiparticle band gaps of both monolayer and few-layer forms to within 0.05 eV (see Ref. [30]). For the GW calculations of SeS_2/2H-MoS_2 heterostructure, $N_B = 896$ (see Ref. [30]).

It is well-known that the quasiparticle gap converges rather slowly with the spatial vacuum separation L_z between the
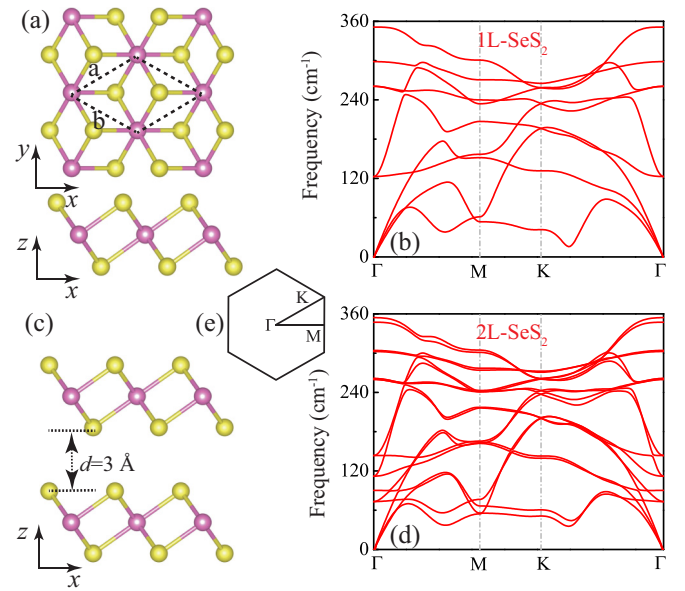
FIG. 1. [(a) and (c)] Top and/or side views of (a) monolayer and (c) bilayer SeS_2 with 1T-MoS_2-like structure. The unit cell is indicated by the black dashed line. [(b) and (d)] Phonon spectrum of monolayer and bilayer SeS_2 obtained at GGA/PBE level of theory. (e) The Brillouin zone with high-symmetry points of few-layer SeS_2.

monolayer and its periodic images because of the nonlocal nature of the GW approximation [31]. The electron-hole interaction is also artificially affected by periodic images over long distances, which tends to significantly affect the exciton binding energy [32]. One way to account for this convergence issue is to use the Coulomb truncation approach [33] that removes image effects directly and leads to well converged results for modest-sized periodic cells. Such a way is very efficient but is currently not implemented in VASP. Since both the quasiparticle gap and optical gap converge as $1/L_z$ [31,34,35], we can extrapolate the gaps to the limit of infinite L_z. This is so-called linear extrapolation scheme. Though computationally more demanding, the extrapolated gaps agree with those from the Coulomb truncation scheme within ~0.05 eV, as tested for other material systems [cf. Ref. [35]]. In our calculations, the latter way is applied in order to accurately determine the quasiparticle and optical gaps. However, due to the slow convergence with respect to L_z in the linear extrapolation scheme, GW calculations may need a careful k-point sampling along z direction. With further convergence test, we find that one k point along z direction is sufficient to obtain well-converged in-direct and direct quasiparticle band gaps within 0.05 eV for $L_z \geqslant 5$ Å.

The quasiparticle band structures at a given L_z are interpolated using maximally localized Wannier functions (MLWF) with the WANNIER90 code [36]. The carrier mobilities are computed using the effective mass approximation coupled with the Boltzmann transport equation and deformation potential theory, considering only the phonon scattering mechanism [5], $\mu_{2D} = \frac{e\hbar^3 C_{2D}}{k_B T (m^* D_\alpha)^2}$, where e is the elemental charge, $\hbar$ is the reduced Planck constant, k_B is the Boltzmann constant, T is the temperature (~300 K), and m^* is the electron or hole effective mass directly computed from the

GW quasiparticle band structure with $L_z = 30$ Å. C_{2D} and D_α are the elastic modulus and deformation potential along the transport direction, both of which are obtained at DFT/PBE level of theory.

The optical properties are determined by employing the Bethe-Salpeter equation (BSE) method within the Tamm-Dancoff approximation [37] on top of GW quasiparticle eigenvalues and wave functions. Through convergence test, we find that considering the lowest nine conduction band states and highest nine valence band states in the BSE calculations is sufficient to reach well-converged results (see Ref. [30]). When the spin-orbit coupling is included, the number of bands involved in solving BSE is doubled. The optical absorbance is calculated by [38,39]

$$A(E) = 1 - e^{-\alpha(E)d_z} = 1 - e^{-2\pi(E/hc)\epsilon_2 d_z}, \quad (1)$$

where $\alpha(E)$ is the absorption coefficient, ϵ_2 is the imaginary part of the dielectric function obtained either by $G_0W_0 + $ BSE or by $G_0W_0 + $ RPA, and d_z is the simulation cell perpendicular to the layers, which includes the atomic layer thickness and the vacuum spatial separation (e.g., L_z). The theoretical upper limit to the conversion efficiency of sunlight to lowest exciton energy P is based on the overlap between the solar spectrum and the optical absorbance [38,39],

$$P = \frac{\int_0^{\lambda_{max}} W(\lambda)A(\lambda)C(\lambda)d\lambda}{\int_0^\infty W(\lambda)d\lambda}, \quad (2)$$

where λ is the photon wavelength and λ_{max} is the longest wavelength that can be absorbed by the ultrathin materials and is determined by the lowest exciton energy E_0, $\lambda_{max} = \frac{hc}{E_0}$, $W(\lambda)$ is the solar spectral irradiance at air mass 1.5. $A(\lambda)$ is the optical absorbance obtained with Eq. (1). $C(\lambda)$ is the conversion factor to account for the fraction of the photon energy converted to the lowest-exciton energy (i.e., the thermalization loss), $C(\lambda) = \lambda \frac{E_0}{hc}$. The phonon spectra is computed using the PHONOPY package [40] with the input forces calculated from the VASP code and is cross-checked with different functionals.

III. RESULTS AND DISCUSSION

A. Structural, electronic, and excitonic properties of SeS$_2$ monolayers

We start with the monolayer SeS$_2$, which is obtained by replacing the Se atoms on the S sites of the 1T-MoS$_2$-like α-selenene structure with S atoms of lighter mass and smaller atomic radius [cf. Fig. 1(a)]. The optimized lattice parameters for monolayer and bilayer SeS$_2$ using various functionals are compiled in Table I, and the detailed atom positions in the unit cell are provided in Table S1. The relaxed lattice parameter at monolayer limit tends to be 6% smaller than its selenene counterpart at the GGA/PBE level of theory. We also provide the relaxed parameters calculated using meta-GGA-SCAN, which is expected to have a closer agreement with future experiments, as has been demonstrated for bulk tellurium [6]. Those parameters are found to have marginal variation from monolayer to bilayer (cf. Table I). The calculated phonon spectra is free of soft phonon modes [cf. Fig. 1(c)], therefore demonstrating that monolayer SeS$_2$ is dynamically stable. The stability nature has been cross-checked and confirmed em-

TABLE I. Lattice constants (in unit of Å) obtained using LDA, GGA/PBE, and meta-GGA-SCAN functionals for monolayer and bilayer SeS$_2$ and TeS$_2$.

Functionals	SeS$_2$		TeS$_2$	
	Monolayer	Bilayer	Monolayer	Bilayer
LDA	3.486	3.496	3.734	3.744
GGA/PBE	3.564	3.565	3.810	3.813
meta-GGA-SCAN	3.528	3.526	3.791	3.791

ploying LDA functional. We note that the distorted T′-phase like for MoS$_2$ is not present for monolayer SeS$_2$.

The quasiparticle band structure obtained at G_0W_0@DFT/PBE level of theory is presented in Fig. 2. We find that monolayer SeS$_2$ appears an indirect band gap
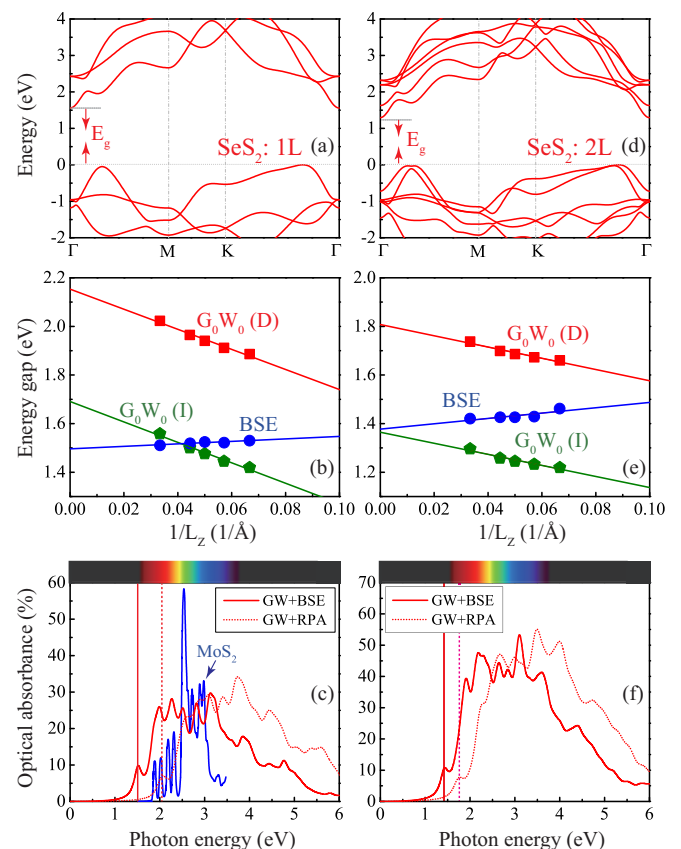
FIG. 2. [(a) and (d)] Quasiparticle band structures of (a) monolayer and (b) bilayer SeS$_2$ obtained at G_0W_0 level of theory with $L_z = 30$ Å. The energy is referenced to the top of the valence band (gray short dotted line). [(b) and (e)] The indirect band gap [$G_0W_0(I)$] and minimum direct band gap [$G_0W_0(D)$] obtained at G_0W_0 level, and the optical gap obtained from BSE calculations (BSE) as a function of the inverse spatial separation L_z for (b) monolayer and (e) bilayer SeS$_2$, respectively. The solid lines represent linear extrapolations. In (c) and (f), the corresponding optical absorbance obtained by GW+BSE (solid lines) and GW+RPA (dotted lines), respectively. The vertical lines indicate the first exciton absorption peak. In (c), the optical absorbance of monolayer MoS$_2$ data is taken from Ref. [42] for comparison purpose.

TABLE II. Carrier effective masses (in unit of m_0), and mobilities (in unit of $cm^2\,V^{-1}\,s^{-1}$) calculated based on G_0W_0 level of theory for monolayer SeS_2 and TeS_2, compared with 2D MoS_2 (Ref. [5]).

Materials	Effective masses		Carrier mobility ($\times 10^3$)	
	Electron	Hole	Electron	Hole
α-SeS_2	0.15	0.27	0.70	0.52
α-TeS_2	0.15	0.23	0.77	0.88
2H-MoS_2	0.47	0.58	0.08	0.29

semiconductor. The valence band maximum (VBM) locates at half-way between Γ and M points, while the CBM locates at the Γ point [cf. Fig. 2(a)]. The indirect gap is determined to be 1.69 eV employing a linear extrapolation at spatial vacuum separation $L_z^{-1} \rightarrow 0$ [cf. $E_g^{G_0W_0(I)}$ of Fig. 2(b)]. We note that this quasiparticle band gap, with self-energy correction, appears nearly twice as large as that obtained at DFT/PBE level ($\sim$0.88 eV). To gain insight into the transport properties of monolayer SeS_2, we calculate the carrier effective masses at the band extremum and the resulted phonon-limited carrier mobilities are shown in Table II. We find that monolayer SeS_2 exhibits extraordinary isotropic electronic transport properties, contrary to the anisotropic nature of 2D black phosphorus of group V [41]. The obtained carrier mobilities are much larger than its 2D MoS_2 analog.

The optical spectroscopy has the significant advantage of being a true "bulk" probe of the electronic structure of a material. In order to access the absorption spectra of monolayer SeS_2, we have calculated the photon-energy dependent imaginary part of the dielectric function from both GW+RPA and GW+BSE levels of theory. The electron-hole interaction, which is important in 2D materials as has been shown by both computations and experiments [41–44], is neglected with the former level of theory, while it is properly accounted for with the latter one. We find that the excitonic effects are significant in monolayer SeS_2 by comparing the results generated from both levels of theory, which reshape substantially the absorption spectra [cf. Fig. 2(c)]. The first absorption peak (i.e., optical gap) appears at photon energy of 1.5 eV, which is originated from the direct transition from the VBM to the conduction band. Remarkably, monolayer SeS_2 demonstrates strong optical absorption across the whole visible-light region [cf. Fig. 2(c)]. The optical gap value combined with the strong visible-light absorption characteristic makes monolayer SeS_2 highly appealing for many device applications, such as light-emitting devices for display and lighting [45–47], and photovoltaics. Indeed, the optical gap of monolayer SeS_2 lies in the ideal energy window of 1.0–1.5 eV corresponding to the maximum photoconversion efficiency in photovoltaic applications. A larger gap value results in nonabsorption of a large portion of photons in the solar spectrum. Whereas if the absorber has a gap value that is too small, most photons have much more energy than necessary to excite electrons across the band gap, resulting in inefficient absorption of the sunlight. Comparing with monolayer MoS_2 which is considered as a good photovotaic material [48], monolayer SeS_2 enables a broader optical absorption covering the whole

visible-light region, and has a larger optical absorbance particular in the lower-energy region [cf. Fig. 2(c)].

The exciton binding energy, defined as the energy difference between the minimum direct quasiparticle gap and the optical gap, is a measure of the nature of the electron-hole pair created during the photoexcitation. Using the linearly extrapolated minimum direct quasiparticle gap of 2.15 eV [cf. $E_g^{G_0W_0(D)}$ of Fig. 2(b)], we obtain a binding energy of 0.66 eV for monolayer SeS_2. This rather high exciton binding energy is a signature of a bound exciton, which implies stability against thermal dislocation of the exciton states that will dominate the room-temperature optical response and nonequilibrium dynamics of monolayer SeS_2. Hence, this property will make monolayer SeS_2 a candidate for light-emitting and photovoltaic devices operating at room temperature. The electronic structure and excitonic properties of SeS_2 are layer-dependent. The indirect band gap is reduced to 1.37 eV [cf. Figs. 2(d) and 2(e)], and a "camelback"-like structure appears at the top of the valence band at bilayer due to the strong interlayer p_z-p_z interaction [cf. Fig. 2(d)]. The first absorption peak experiences a redshift comparing with the monolayer counterpart, and it appears at photon energy of 1.38 eV obtained from the linear extrapolation technique [cf. Fig. 2(e)]. The binding energy decreases to 0.43 eV. It is interesting to find that bilayer SeS_2 also exhibits strong optical absorbance, covering the whole visible-light region [cf. Fig. 2(f)].

B. Structural, electronic, and excitonic properties of TeS_2 monolayers

Next, we turn to monolayer TeS_2. Its geometric structure is built in a similar manner as the aforementioned SeS_2 monolayer, i.e., replacing the Te atoms on the S-sites of the 1T-MoS_2-like α-tellurene structure with S atoms. The lattice parameter of TeS_2 (cf. Table I) appears larger than its SeS_2 counterpart but smaller than that of α-tellurene ($\sim$4.15 Å at GGA/PBE level of theory). The relaxed parameters exhibit marginal variation from monolayer to bilayer (cf. Table I). Phonon spectra of monolayer TeS_2 is found to be free of soft-phonon modes, therefore suggesting that it is mechanically stable [cf. Fig. 3(a)]. Monolayer TeS_2 also possesses extraordinary carrier mobilities, favoring ultrafast electronic transport (cf. Table II).

Comparing to monolayer SeS_2, one of the unique characteristic of TeS_2 is its heavy-element containing feature. The impact of spin-orbit coupling (SOC) therefore should be carefully examined. The quasiparticle band structures both with and without spin-orbit interaction resembles very much its SeS_2 counterpart [cf. Fig. 3(b)]. Without SOC, the indirect band gap of monolayer TeS_2 reduces to 1.37 eV comparing to monolayer SeS_2 [cf. Fig. 2(b)]. We note that this gap value remains more than twice as much as that obtained from the DFT/PBE level of theory ($\sim$0.53 eV). When the SOC is switched on, three resulted characteristics in the quasiparticle band structures are observed. (i) The SOC has considerable effects on the conduction band structures. It splits the degenerate bands at high-symmetry k points [e.g., Γ point, cf. Fig. 3(b)]. However, the SOC has nearly no impact on the valence band structures (at lease those close to the valence band maximum (VBM)). This is because the topmost valence
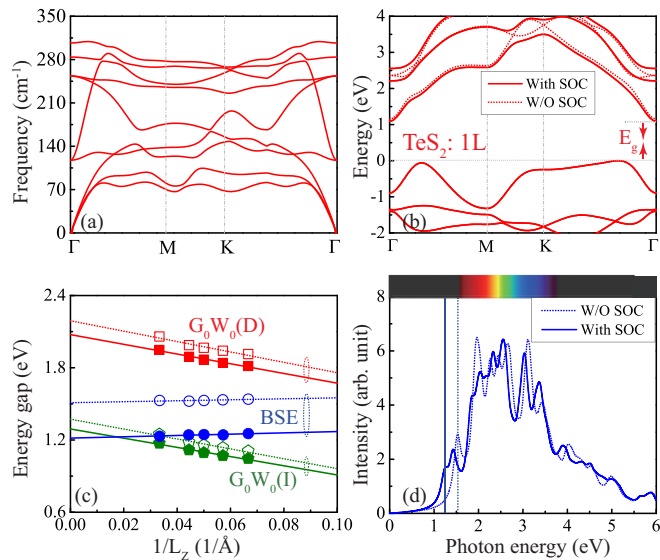
FIG. 3. (a) Phonon spectra of monolayer TeS_2. (b) Quasiparticle band structure of monolayer TeS_2 with (solid line) and without (dotted line) considering the spin-orbit coupling, obtained at G_0W_0 level of theory with $L_z = 30$ Å. The energy is referenced to the top of the valence band (gray short dotted line). (c) The indirect band gap [$G_0W_0(I)$] and minimum direct band gap [$G_0W_0(D)$], and the optical gap as a function of the inverse spatial separation L_z for monolayer TeS_2, respectively, without (open symbols) and with (filled symbols) considering the spin-orbit interaction. The lines represent linear extrapolations. (d) The corresponding absorption spectrum obtained by GW+BSE method, neglecting (dotted lines) or considering (solid lines) the spin-orbit interaction, respectively, at $L_z = 30$ Å. The vertical lines indicate the first exciton absorption peak.

FIG. 4. (a) The optical gap of few-layer SeS_2 and TeS_2 as a function of the number of layers. Each solid line represents a power law fit of the numerically calculated values (symbols). The results of 2D black phosphorus (BP, Ref. [49]) and MoS_2 (Ref. [50]) are plotted for comparisons. The dotted line connecting the data points of 2D MoS_2 represents a guide for the eye. The shadow area represents the optimal energy window for single pn-junction photovoltaic applications [51]. (b) The exciton binding energy as a function of the minimum direct band gap of few-layer SeS_2 and TeS_2 materials. Each solid line represents a linear fit, and the number of layers are marked alongside. (c) Quasiparticle band structure and (d) optical absorption spectrum of SeS_2/2H-MoS_2 van der Waals heterostructure obtained using G_0W_0@DFT/PBE level of theory with $L_z = 20$ Å. The vertical lines in (d) indicate the first exciton absorption peak.

band states are dominantly originated from the *p*-orbital of lighter S atoms, and the low-lying conduction band counterparts have nearly an equal contribution from the *p*-orbitals of both the lighter S atoms and the heavier Te atoms. (ii) The SOC reduces both the indirect and direct gaps to 1.29 and 2.076 eV, respectively. (iii) The excitonic effects are also important in monolayer TeS_2, and SOC appears significantly impact the near-band-edge optical absorption, including both the absorption position and intensity. Comparing to the quasiparticle gaps, the effect of SOC on the optical gap is much larger, red-shifting the optical gap from 1.51 eV (close to that of monolayer SeS_2, without SOC) to 1.22 eV [with SOC, cf. Fig. 3(d)]. This leads to an increased exciton binding energy of 0.86 eV comparing to that in the absence of SOC (~0.68 eV). Remarkably, monolayer TeS_2 also demonstrates strong optical absorbance in the whole visible-light region, irrespectively of the impact of SOC [cf. Fig. 3(d)].

C. Layer-dependent excitonic characteristics of few-layer SeS_2 and TeS_2

Both SeS_2 and TeS_2 at monolayer limit have shown to exhibit appealing excitonic properties, such as suitable absorption edge and strong visible-light absorbance nature. It is therefore imperative to examine how those properties vary against the number of layers, and compare with those of 2D MoS_2 and black phosphorus (BP) analogs. Prior to the presen-

tation of excitonic properties, we take bilayer SeS_2 and TeS_2 as prototype systems to examine the structural stability of both materials in their few-layer forms. We find that the calculated phonon spectrum of those bilayers is free of soft phonon modes (cf. Fig. 1(d) and Ref. [30]), therefore demonstrating their dynamic stability.

The layer-dependent optical gaps are shown in Fig. 4(a). We find that the absorption edge of those two newly discovered 2D materials of group VI is tunable via the number of layers involved in the stack, contrary to their 2D MoS_2 counterpart. Remarkably, the optical gaps of few-layer SeS_2 remain in the optimal energy window of 1.0–1.5 eV (shadow area) that corresponds to the maximum photoconversion efficiency for single *pn*-junction photovoltaic applications [51]. The conversion efficiency of bilayer SeS_2 is calculated and found to exceed 10%, which outperforms the conversion limit of $Cu_2ZnSn(S, Se)_4$ [51]. This remarkable efficiency upper limit achieved with thickness of less than 1 nm of few-layer SeS_2 and is comparable to the current efficiency records realized with organic and dye-sensitized solar-cell technologies.

A power-law fit $E_g^{opt} = \alpha/N^\gamma + \delta$, with N being the number of layer and α, γ and δ being the fitting parameters, is applied in Fig. 4(a). We find $\gamma = 1.3$ and 0.93 for few-layer SeS_2 and TeS_2, respectively, both of which appear considerably smaller than the usual quantum confinement result (~$1/N^2$). This is attributed to the interplay between the 2D

quantum confinement effects, interlayer coupling, and many-body effects. Comparing to 2D black phosphors of group V, the optical gaps of both few-layer SeS_2 and TeS_2 decay slower as a function of the number of layers [cf. Fig. 4(a)].

Large binding energy, due to the extreme 2D nature of carrier confinement and reduced screening, prevents the exciton dissociation against thermal noise, therefore being highly favorable for exciton-manipulation related fundamental study and device applications, such as exciton condensation. However, it is also *a priori* disadvantage for the applications like photovoltaics, for which a fast charge separation (e.g., fast "exciton dissociation") is a prerequisite. Fortunately, we find that the binding energy of the bound exciton can be effectively tuned by the number of stacked layers for both few-layer SeS_2 and TeS_2 [cf. Fig. 4(b)]. Indeed, the exciton binding energy for a quad-layer SeS_2 is reduced to nearly 25% of its monolayer counterpart (~0.66 eV), while keeping the optical gap in the optimal energy window [cf. Fig. 4(a)]. Finally, we found that the exciton binding energy has a linear correlation with both the indirect and direct gaps [cf. Fig. 4(b)], which agrees well with the universal linear scaling law correlating the exciton binding energy with the band gap of various 2D materials [35,52,53].

D. Engineering the indirect band gap nature via van der Waals heterostructure

Direct gap semiconductor usually performs much better in the photovotaic applications than its indirect gap counterpart [cf. Ref. [48]]. It is therefore worthwhile to explore an effective way of manipulating the band gap nature of those newly discovered monolayers of group VI to boost related device performances. We take monolayer SeS_2 as an example, and tentatively combine it with one of most well-studied group of 2D materials, transition metal dichalcogenides, to form the 2D van der Waals heterostructure. This type of structure is known to not only preserve the intrinsic properties of corresponding components, but also induce new properties. Among those transition metal dichalcogenides, we find that SeS_2/2H-MoS_2 heterostructure indeed delivers a direct-gap nature [see Fig. 4(c)]. When constructing this heterostructure, we have used a $\sqrt{3} \times \sqrt{3}$ supercell of monolayer SeS_2, and 2×2 cell of monolayer 2H-MoS_2, which leads to a tolerable lattice match of $\sim3\%$ and 48 atoms in total per cell. The direct gap is found to be ~0.81 eV at PBE level of theory without SOC, and opened up to 1.09 eV when including the self-energy correction at G_0W_0/PBE level of theory [cf. Fig. 4(c)]. This quasiparticle gap appears slightly smaller than that obtained using the HSE06 hybrid functional (~1.23 eV), but remains within the aforementioned optimal energy window of 1.0–1.5 eV. The SOC has negligible impact on the band gap, reducing the gap by only 0.07 eV at PBE level of theory.

Finally, we evaluate the excitonic properties of SeS_2/2H-MoS_2 heterostructure in Fig. 4(d). The first exciton (e.g., optical gap) appears at photon energy of 0.75 eV, which contributes dominantly from the direct transition from the CBM to VBM. Although being optically bright, the oscillator strength of such an exciton is weak [cf. Fig. 4(d)]. This can be understood from the analysis of the partial density of states

(PDOS) of the heterostructure. The CBM is found to mainly contribute from an equal contribution from the p-orbitals of Se and S atoms of monolayer SeS_2, while the VBM mainly derives from the d-orbital of Mo atoms of monolayer MoS_2. This results in the charge density localization of CBM and VBM states nearly separately in the SeS_2 and MoS_2 regions. Such a spatial separation might suggest the interlayer nature of the first exciton state, and is responsible for the weak oscillator strength. In this context, strong charge separation not only promotes the dissociation of excitons into free electrons and holes, but also significantly reduces the electron-hole recombination rates, which may contribute to the long minority carrier lifetime [54]. The excitonic effects remain significant in the heterostructure [cf. Fig. 4(d)]. Due to the enhanced screening effects, the exciton binding energy of the heterostructure (~0.34 eV) appears smaller than both monolayers of SeS_2 (~0.66 eV) and MoS_2 (~0.96 eV [Ref. [42]]). The first pronounced exciton state peaks at photon energy of 1.42 eV, and exhibits an oscillator strength a few order of magnitude larger ($\sim10^5$) than the first optically bright exciton state [as indicated by vertical arrow of Fig. 4(d)]. Remarkably, the heterostructure exhibits strong optical absorption across the whole visible light region.

IV. CONCLUSIONS

We have reported two new 2D materials of group VI, namely, monolayer SeS_2 and TeS_2 with 1T-MoS_2-like structure, which are mechanically stable. Using the GW-BSE approach, we have accurately determined the quasiparticle band structures and excitonic properties of these two 2D materials. We find that those newly discovered 2D materials are indirect semiconductors and possess extraordinary electronic transport properties with isotropic carrier mobilities. The exciton appears strongly bound and stable at room temperature with a binding energy of 0.66 and 0.84 eV for monolayer SeS_2 and TeS_2, respectively. The optical gap of these two monolayer materials lies in the ideal energy window of 1.0–1.5 eV corresponding to the maximum photoconversion efficiency, and their absorption spectra covers the whole visible-light region, which, to certain extent, immune to the fluctuation of layer thickness. Finally, we propose the formation of SeS_2/2H-MoS_2 van der Waals heterostructure can serve as an effective mean to turn the indirect band nature of monolayer SeS_2 into a direct nature. Those characteristics make few-layer SeS_2 and TeS_2 highly appealing for room-temperature optoelectronic devices, such as light-emitting devices for display and lighting, and photovoltaic devices.

[1] K. S. Novoselov, A. K. Geim, S. V. Morozov, D. Jiang, Y. Zhang, S. V. Dubonos, I. V. Grigorieva, and A. A. Firsov, Science **306**, 666 (2004).

[2] C.-C. Liu, W. Feng, and Y. Yao, Phys. Rev. Lett. **107**, 076802 (2011).

[3] L. Li, Y. Yu, G. J. Ye, Q. Ge, X. Ou, H. Wu, D. Feng, X. H. Chen, and Y. Zhang, Nat. Nanotechonol. **9**, 372 (2014).

[4] H. Liu, A. T. Neal, Z. Zhu, Z. Luo, X. Xu, D. Tománek, and P. D. Ye, ACS Nano **8**, 4033 (2014).

[5] Z. Zhu, X. Cai, S. Yi, J. Chen, Y. Dai, C. Niu, Z. Guo, M. Xie, F. Liu, J.-H. Cho, Y. Jia, and Z. Zhang, Phys. Rev. Lett. **119**, 106101 (2017).

[6] S. Yi, Z. Zhu, X. Cai, Y. Jia, and J.-H. Cho, Inorg. Chem. **57**, 5083 (2018).

[7] Y. Wang, G. Qiu, R. Wang, S. Huang, Q. Wang, Y. Liu, Y. Du, W. A. Goddard, M. J. Kim, X. Xu, P. D. Ye, and W. Wu, Nat. Electron. **1**, 228 (2008).

[8] D. Liu, X. Lin, and D. Tománek, Nano Lett. **18**, 4908 (2018).

[9] J. Min, C. Zhao, Z. Zeng, Y. Jia, and Z. Du, Phys. Rev. B **100**, 085402 (2019).

[10] Q. Gao, X. Li, L. Fang, T. Wang, S. Wei, C. Xia, and Y. Jia, Appl. Phys. Lett. **114**, 092101 (2019).

[11] J. Chen, Y. Dai, Y. Ma, X. Dai, W. Ho, and M. Xie, Nanoscale **9**, 15945 (2017).

[12] Y. Pan, S. Gao, L. Yang, and J. Lu, Phys. Rev. B **98**, 085135 (2018).

[13] S. Sharma, N. Singh, and U. Schwingenschlögl, ACS Appl. Energy Mater. **1**, 1950 (2018).

[14] Z. Gao, F. Tao, and J. Ren, Nanoscale **10**, 12997 (2018).

[15] Y. Chen, J. Liu, J. Yu, Y. Guo, and Q. Sun, Phys. Chem. Chem. Phys. **21**, 1207 (2019).

[16] Y. Liu, W. Wu, and W. A. Goddard, J. Am. Chem. Soc. **140**, 550 (2018).

[17] Y. Wang, C. Xiao, M. Chen, C. Hua, J. Zou, C. Wu, J. Jiang, S. A. Yang, Y. Lu, and W. Ji, Mater. Horiz. **5**, 521 (2018).

[18] Z. Gao, G. Liu, and J. Ren, ACS Appl. Mater. Inter. **10**, 40702 (2018).

[19] S. Tutihasi, G. G. Roberts, R. C. Keezer, and R. E. Drews, Phys. Rev. **177**, 1143 (1969).

[20] C. Liu, T. Hu, Y. Wu, H. Gao, Y. Yang, and W. Ren, J. Phys.: Condens. Matter **31**, 235702 (2019).

[21] J. Qin, G. Qiu, J. Jian, H. Zhou, L. Yang, A. Charnas, D. Y. Zemlyanov, C.-Y. Xu, X. Xu, W. Wu, H. Wang, and P. D. Ye, ACS Nano **11**, 10222 (2017).

[22] P. E. Blöchl, Phys. Rev. B **50**, 17953 (1994).

[23] G. Kresse and J. Furthmüller, Phys. Rev. B **54**, 11169 (1996).

[24] G. Kresse and J. Hafner, Phys. Rev. B **49**, 14251 (1994).

[25] G. Kresse and D. Joubert, Phys. Rev. B **59**, 1758 (1999).

[26] J. P. Perdew, K. Burke, and M. Ernzerhof, Phys. Rev. Lett. **77**, 3865 (1996).

[27] J. H. Yang, D. A. Kitchaev, and G. Ceder, Phys. Rev. B **100**, 035132 (2019).

[28] S. Grimme, J. Comput. Chem. **27**, 1787 (2006).

[29] T. Kerber, M. Sierka, and J. Sauer, J. Comput. Chem. **29**, 2088 (2008).

[30] See Supplemental Material at http://link.aps.org/supplemental/10.1103/PhysRevMaterials.4.104004 for details regarding the atomic posisitons of monolayer SeS_2 and TeS_2, convergence test resukts of *GW* and BSE calcualtions, and phonon spectra of monolayer TeS_2.

[31] N. Berseneva, A. Gulans, A. V. Krasheninnikov, and R. M. Nieminen, Phys. Rev. B **87**, 035404 (2013).

[32] C. Wagner, J. Schuster, and A. Schleife, Phys. Rev. B **99**, 075140 (2019).

[33] S. Ismail-Beigi, Phys. Rev. B **73**, 233103 (2006).

[34] J. P. A. Charlesworth, R. W. Godby, and R. J. Needs, Phys. Rev. Lett. **70**, 1685 (1993).

[35] J.-H. Choi, P. Cui, H. Lan, and Z. Zhang, Phys. Rev. Lett. **115**, 066403 (2015).

[36] A. A. Mostofi, J. R. Yates, G. Pizzi, Y.-S. Lee, I. Souza, D. Vanderbilt, and N. Marzari, Comput. Phys. Commun. **185**, 2309 (2014).

[37] T. Sander, E. Maggio, and G. Kresse, Phys. Rev. B **92**, 045209 (2015).

[38] G. Shi and E. Kioupakis, ACS Photonics **2**, 208 (2015).

[39] G. Shi and E. Kioupakis, Nano Lett. **15**, 6926 (2015).

[40] A. Togo and I. Tanaka, Scripta. Mater. **108**, 1 (2015).

[41] J. Qiao, X. Kong, Z.-X. Hu, F. Yang, and W. Ji, Nat. Commun. **5**, 4475 (2014).

[42] D. Y. Qiu, F. H. da Jornada, and S. G. Louie, Phys. Rev. Lett. **111**, 216805 (2013).

[43] P. Johari and V. B. Shenoy, ACS Nano **5**, 5903 (2011).

[44] T. Cheiwchanchamnangij and W. R. L. Lambrecht, Phys. Rev. B **85**, 205302 (2012).

[45] H. Shen, Q. Gao, Y. Zhang, Y. Lin, Q. Lin, Z. Li, L. Chen, Z. Zeng, X. Li, Y. Jia, S. Wang, Z. Du, L. S. Li, and Z. Zhang, Nature Photon. **13**, 192 (2019).

[46] H. Zhang, N. Hu, Z. Zeng, Q. Lin, F. Zhang, A. Tang, Y. Jia, L. S. Li, H. Shen, F. Teng, and Z. Du, Adv. Opt. Mater. **7**, 1801602 (2019).

[47] H. Zhang, X. Ma, Q. Lin, Z. Zeng, H. Wang, L. S. Li, H. Shen, Y. Jia, and Z. Du, J. Phys. Chem. Lett. **11**, 960 (2020).

[48] D. Jariwala, A. R. Davoyan, J. Wong, and H. A. Atwater, ACS Photonics **4**, 2962 (2017).

[49] V. Tran, R. Soklaski, Y. Liang, and L. Yang, Phys. Rev. B **89**, 235319 (2014).

[50] H.-P. Komsa and A. V. Krasheninnikov, Phys. Rev. B **86**, 241201(R) (2012).

[51] P. D. Matthews, P. D. McNaughter, D. J. Lewis, and P. O'Brien, Chem. Sci. **8**, 4177 (2017).

[52] T. Olsen, S. Latini, F. Rasmussen, and K. S. Thygesen, Phys. Rev. Lett. **116**, 056401 (2016).

[53] Z. Jiang, Z. Liu, Y. Li, and W. Duan, Phys. Rev. Lett. **118**, 266401 (2017).

[54] J. Ma and L.-W. Wang, Nano Lett. **15**, 248 (2015).